ANTIOXIDANTS & REDOX SIGNALING
Volume 9, Number 8, 2007

DOI: 10.1089/ars.2007.1643

Forum Review

Developments in Quantitative Oxygen-Saturation Imaging of Breast Tissue *In Vivo* Using Multispectral Near-Infrared Tomography

SUBHADRA SRINIVASAN,[1] BRIAN W. POGUE,[1] COLIN CARPENTER,[1] SHUDONG JIANG,[1] WENDY A. WELLS,[2] STEVEN P. POPLACK,[3] PETER A. KAUFMAN,[3] and KEITH D. PAULSEN[1,3]

ABSTRACT

Imaging of oxygen saturation provides a spatial map of the tissue metabolic activity and has potential in diagnosis and treatment monitoring of breast cancer. Oxygen-saturation imaging is possible through near-infrared (NIR) tomography, but has low signal-to-noise ratio (SNR). This can be augmented by using NIR tomography as an add-on to MRI. Presented are results from a free-standing NIR system and a hybrid MR-guided system for breast imaging. In results from imaging 60 healthy volunteers in the initial NIR system, oxygen saturation was a significant discriminator between the BIRADS classifications of adipose tissue, heterogeneously dense, and extremely dense tissue. By using the MR-guided NIR system, more accurate tissue-specific data were obtained on adipose and fibroglandular volumes, with 11 healthy volunteers. In these data, oxygen saturation in the adipose tissue correlated with percentage of adipose tissue. In two case studies of infiltrating ductal carcinomas, oxygen saturation was reduced at the site of the tumor, as compared with the surrounding healthy tissue, agreeing with conventional thought that hypoxia exists in larger solid tumors. The MRI-guided NIR images of oxygen saturation provide higher resolution and superior SNR and will likely be used in the future to study and characterize specific tissue volumes. *Antioxid. Redox Signal.* 9, 1143–1156.

INTRODUCTION TO NIR SPECTROSCOPY AND TOMOGRAPHY

Absorption of NIR bands of light by oxyhemoglobin (HbO_2) and deoxyhemoglobin (HbR) and water in breast tissue is low enough to allow penetration and hence imaging of up to a dozen centimeters into tissue (5). Light propagation through tissue in this wavelength band is scatter-dominated, and these scattering events occur because of differences in the index of refraction between cell organelles and across membranes. By sampling light reflectance and transmittance around the breast at multiwavelengths, and by using a suitable model for light propagation along with known spectral signatures, two-dimensional (2-D) and three-dimensional (3-D) images of a functional nature directly relating to vascular and molecular architecture of the breast are obtained (22, 43). These images comprise typically five parameters, which in 2-D are coronal slice images of (a) the concentration of total hemoglobin; (b) concentration of water; (c) the oxygen saturation; (d) the scatter amplitude; and (e) the scatter power. The latter two parameters are obtained from an empiric Mie theory approximation to the shape of the reduced scattering spectrum. More recently it has been shown that the scatter power and density can be converted into average scatter particle size and particle density (79,

[1]Thayer School of Engineering, Dartmouth College, Hanover, New Hampshire.
[2]Department of Pathology and [3]Department of Diagnostic Radiology, Dartmouth Medical School, Lebanon, New Hampshire.

80). The total hemoglobin images [Hb_T] are defined as ([HbO_2] + [HbR], millimolar), and the oxygen saturation S_tO_2 is given as [HbO_2]/[Hb_T] in percentages.

Each of these parameters provides a subtly different measure of the status of the tissue. Much of the focus of development in this area has been on imaging malignancies, which have high amounts of neovasculature resulting in increased hemoglobin content, when compared with normal tissue (56, 72). The conventional view is that an increased demand for oxygen supply is present in the tumor, resulting in lower oxygenation (31, 77), and this is observable from NIR imaging because the supply of oxygenated blood is lower than the demand for supplying oxygen, and the overall bulk tissue value of oxygen saturation appears lower. Cancer cells stimulate rapid endothelial cell proliferation, and on a cellular level, differences between cancers and normal tissue include multinucleation, structural distortion, and membrane and mitochondrial variations (72). All these result in changes in scattering with wavelength.

Tomography with light in the NIR wavelength band has the ability to provide low-resolution images directly relating to the vascular and cellular makeup of tissue. This complements traditional imaging techniques, which rely primarily on the structural architecture of tissue to provide information. Whereas NIR optical tomography has found research applications in the study of brain function (30, 32, 70), and skin (45), muscle (27) and breast tissue (56, 72), it could also have a unique niche in diagnostic imaging for breast cancer. NIR spectral tomography provides a different perspective through the vascular images that can reduce the numbers of these biopsies. A current area of research, which may prove to be the major pathway for NIR to be introduced into current clinical practice, is through coupling with existing imaging systems. For example, MRI is the most advanced modality to image complex breast tissues and has extremely good sensitivity, yet suffers from moderate specificity, leading to high false-positive rates (25, 50), which ultimately results in larger numbers of unnecessary biopsies of benign lesions. Using NIR in addition to MRI is discussed here and shown to provide more information, such as oxygen saturation, to the imaging-system capability.

Role of oxygen saturation in breast cancer diagnosis and treatment:

The role of oxygen saturation in diagnosis has been well theorized (31) but elusive to measure and interpret. As a solid tumor progresses, angiogenesis produces a leaky and abnormal vasculature that is characterized by hypervascularity at the tumor periphery, whereas the tumor center can be hypovascular (40). The hypoxic fraction that develops at the core of the tumor because of the metabolic imbalance between oxygen supply and consumption, as well as pressure buildup, cannot be predicted on the basis of tumor stage or grade (76), although it does depend critically on the whole-blood hemoglobin levels (78). Hypoxia also relates to therapeutic concerns for cancers: response to radiotreatment (49) and prognosis and metastasis (6). In addition, the oxygenation of fibroglandular tissue itself may be different from less metabolically active adipose tissue. This complicated picture of oxygen saturation as a diagnostic parameter has been reflected in numerous studies. Recent publications (16, 18, 29, 34, 64, 66) have shown results from multicenter clinical trials using a range of NIR imaging/spectroscopy techniques and differing numbers of wavelengths (lower limit, 2 wavelengths; upper limit, steady-state broadband spectra), with two of the studies (29, 64) involving a number of subjects ($N > 100$). Whereas deoxyhemoglobin concentration was shown to be a significant discriminator in some of these studies (16, 34), oxygen saturation itself has not been a statistically significant discriminator in any of them, between malignant and normal/benign tissue. Chance *et al*. (18) showed that oxygen saturation, when combined with total hemoglobin, could give sensitivity and specificity figures of 96% and 93%, respectively, for detection of malignant relative to benign tissue. By using NIR spectroscopy to follow a patient responding to neoadjuvant chemotherapy, oxygen saturation was found to increase over a 10-week course of treatment (35). In an alternate study evaluating the potential of NIR tomography to monitor treatment, total hemoglobin decreased with treatment cycles, corresponding to tumor-volume decrease; oxygen saturation also decreased significantly after the fifth cycle (20). Other than Spinelli *et al*. (64), who used size estimates from histopathology to recover images, none of the other studies used information from any other imaging modality in image reconstruction.

Ratiometry for oxygen-saturation measurement and extension to imaging

Oxygen-saturation measurements at microscopic levels are possible through a variety of techniques: Eppendorf electrodes, laser Doppler flowmetry, cryospectrophotometry, and polarographic measurements, to name a few (23). These techniques provide localized measurements mostly on experimental tissues, and some, only on *ex vivo* samples. At a macroscopic level, oxygen saturation of arterial blood can be measured routinely through pulse oximeters, which rely on sampling the absorption of oxy and deoxyhemoglobin at two wavelengths (usually 660 and 940 nm), and having a self-calibrating way to assess the oxygenation based on the ratio of absorbances on and off of the pulsatile flow of the artery. Pulse oximeters are used widely to monitor arterial oxygen-saturation levels in patients undergoing anesthesia, surgery, intensive care, and asthma, *etc*. (47). The principle of the oximeter is strictly valid only for pulsatile flow, such as is observed in the arteries, and when suitably calibrated, they yield measurements with high signal-to-noise ratio (SNR). The use of ratiometric data is a stable way to measure, assuming stable light sources such as diode lasers or light-emitting diodes. However, movement artifact or poor coupling to the tissue are the two largest problems in use of these devices, as the light transmission through the tissue is significantly affected by the tissue geometry and the surface shape of the tissue.

Imaging of oxygen saturation without reference to pulsatile flow requires a model-based interpretation of the measurements, and diffusion theory–based simulation of the light propagation is almost universally used because of its ability to produce tractable solutions. NIR tomography with multiple wavelengths has been implemented in many forms with varying numbers of wavelengths, geometries, and source-detector functionalities.

Much focus has been placed on directly measuring the optical path length through tissue by using time-resolved or frequency-domain spectroscopy, and using these information-rich data to predict the absorption coefficients quantitatively at multiple wavelengths, and then estimating the hemoglobin values from this. Unfortunately, this approach does not lend itself well to ratiometric methods, because multiple measurements are used with the model-based recovery of parameters, and when the absorption coefficients are recovered, the averaging of the noise reduces the ability to use ratio data. However, spectral fitting with constraints placed on the bounds of possible hemoglobin concentrations and oxygen-saturation values provides a very workable solution.

Strengths and weaknesses of NIR oxygen-saturation imaging

Quantitative NIR spectroscopy studies of bulk homogeneous tissues such as muscle have shown great promise and accuracy in reporting blood oxygen–saturation values (14, 27), and as such, the potential information from NIR spectroscopy seems rich and very useful. The problems associated with NIR imaging all become more apparent when the tissues studied are inhomogeneous (19, 33, 37, 71, 85) and when the spectral resolution of the instrument is lower. Imaging inherently requires more measurements than spectroscopy, which can be achieved with a single-measurement data set (67, 68). Imaging with NIR is inherently ill posed, because of the diffuse propagation, and so the ability to accurately image different tissue volumes is modest, and becomes worse as the tissue volume becomes smaller and more deeply located. Additionally, many studies have focused on technologic designs that use only a few wavelengths, for simplicity and cost reasons, yet it is becoming apparent that the ability to image oxygen saturation with only a few wavelengths in a complex tissue volume is very poor (68). Yet although the accuracy is low, the repeatability is high (57, 63), such that these systems can be used to track relative changes in response in functional studies of tissue.

The ideal NIR system would use multiple wavelengths of light, obtaining broadband data sets across a large range of the usable spectrum from 650 to 950 nm (12, 82, 83). The ideal system would also not focus too much on trying to image, but rather on using regions defined by something else, and simply reconstruct oxygen-saturation values of several predefined regions. This concept of using prior information from another modality such as MRI appears strong, although clearly it makes sense only if use of that secondary imaging modality is feasible (8, 48, 84).

NIR Spectroscopy and tomography as an add-on to MR imaging

A multimodality MR-guided NIR optical tomography system has been developed and is being evaluated as a potential way to use prior information from the MRI to recover well-defined volumes of oxygen saturation. The concept of combining NIR with MRI is not really to improve NIR *per se*, but rather that NIR can add functional information to that which MRI does not already have. The use of MRI for screening of high-risk population and diagnosis holds promise because of its high sensitivity (26, 28, 38, 39, 41, 50, 51). However, reported specificity figures for MRI vary from 37 to 97% (50), and most positively-enhancing features in a breast MRI examination require additional biopsy, thereby limiting the cost-effectiveness of the examination. NIR imaging provides unique information relating to the metabolic and vascular status of the breast regions and could be used to characterize regions that enhance with MRI. Whereas NIR imaging by itself has from poor resolution and limited penetration, prior structural knowledge can significantly enhance the quantitative estimation of the values (55, 61). MR imaging can clearly image factors related to blood oxygen, as studied extensively in the blood-oxygen level–dependent (BOLD) effect imaging done in functional tissue-activation studies, in which blood-oxygen changes can be quantified in large tissue regions because of the magnetic moment of deoxyhemoglobin. This effect is useful in measuring changes in deoxyhemoglobin and yet is not well calibrated in diseased tissues, where the blood oxygenation changes are not independent of the blood-volume changes. Still given sufficient imaging time, MRI can also be used to image flow, water diffusion, or specific spectroscopic parameters of magnetic nuclei. NIR, although quite different, has, in comparison, high sensitivity but less spatial resolution.

A hybrid approach using NIR tomography as a moderate-cost add-on to traditional MR systems has been developed to counteract these limitations and is attractive for its vascular sensitivity, with high intrinsic contrast (53) and potentially high resolution from the MR images (11). Combining NIR imaging into standard MR examinations could improve sensitivity and reduce the current high false-positive rates of MRI. Potentially, this multimodality system could overcome low-SNR problems with oxygen-saturation imaging and provide more accurate characterization of diseased and normal tissue; it is currently being evaluated in clinical studies for this role.

Outline of this article

In this article, a review of the capabilities of a stand-alone NIR optical tomography system are outlined, as well as a unique hybrid MR system with the NIR instrument added on. Both these systems have been well characterized through experimental studies (11, 44) and have been used to image human subjects (9, 66) in clinical trials at the Dartmouth Hitchcock Medical Center. The oxygen-saturation results are shown as an indicator of the ability to image the influence of low partial pressures of oxygen in tissue with NIR signals. Also shown are statistically significant correlations of oxygen saturation to radiographic density of breast tissue *in vivo* from a study of 60 healthy subjects, and the oxygen saturation and tissue composition *in vivo* from 11 healthy subjects are shown by using the hybrid MR-guided optical system. Case studies of volunteers with malignancies have been analyzed by using both systems to study the heterogeneity in the functional images for subjects with cancers. Although NIR is not used clinically for breast imaging, it has gained acceptance in niche uses for brain imaging and will likely succeed in breast-cancer imaging in the near future.

METHODS AND MATERIALS

Stand-alone NIR optical tomography system

The stand-alone NIR system built at Dartmouth and documented by McBride *et al.* (42, 43) is a multiwavelength frequency-domain instrument allowing amplitude and phase measurements around the periphery of the breast. In brief, the automated NIR tomography device was constructed to obtain anatomically coronal slices of the breast by means of fiberoptic bundles. The fibers are arranged in a circular array (with both radial and vertical degrees of freedom) and have the capability to collect data in three slices of tissue from sets of 16 source and 15 detector locations (see Fig. 1). Intensity-modulated light (at 100 MHz) at six discrete wavelengths between 660 and 850 nm is used to allow multispectral interrogation of the breast. Detection is accomplished by high-gain, high-bandwidth photomultiplier tubes, and the detected light is electrically mixed with a reference signal to yield a low-frequency (500 Hz) signal that is recorded by the computer. The measured data are calibrated to account for small offsets due to source-detector fiber transmission, alignment characteristics, and errors in discretization or model–data mismatch. By fitting the measurements to a homogeneous calculation of the diffusion equation on a circular geometry (of relevant size), an initial estimate of the optical properties can be obtained. This initial estimate is used in the reconstruction on which the calibrated data are processed by a finite-element model of the optical-diffusion equation in the frequency domain (52).

MR-guided NIR tomography system

The NIR system was designed as an add-on to MRI so that frequency-domain measurements at multiple wavelengths can be obtained simultaneously with the MRI examination as the subject lies prone in the magnet. Details of the system have been described elsewhere (11). In brief, the optical instrumentation uses long silica fibers for light transmission at six wavelengths (660–850 nm). Similar to the stand-alone system, intensity-modulated light is passed through each source fiber (total of 16 sources) and corresponding 15 detector fibers that record light measurements after interaction with tissue, by using high-gain photomultiplier tubes. The fibers extend into the body of the 1.5-T whole-body MRI and interrogation of up to 12 cm of tissue is anticipated, with flexible positioning along vertical direction to obtain multiple coronal slices of measurements. Figure 2a shows the electronics of the optical system, which stays outside the room housing the MR unit. Figure 2b shows the circular configuration of the source-detector fibers, and a volunteer being imaged in this hybrid system is shown in Fig. 2c.

Image reconstruction

With these measurements, imaging is carried out by using algorithms based on a finite-element model to the diffusion equation (22, 52) for both systems. Both systems also use spectral priors relating to absorption shapes of the dominant chromophores in the breast tissue and behavior of scatterers in the NIR wavelength band to compute the images (69). This is done by using multiwavelength data simultaneously to reconstruct directly for total hemoglobin, oxygen saturation, water content (in percentage), as well as scattering parameters given by scatter amplitude and scatter power defined from the relation ($\mu_s' = A\lambda^{-b}$ where μ_s' is the reduced scattering coefficient as a function of wavelength λ and A is the amplitude, b is scatter power in this power relation) (46, 74). Spectral priors have been shown to reduce crosstalk between the images as well as the sensitivity to noise in the measurements (21, 69). For the MR-guided optical system, the theoretic formulation has been modified to incorporate the spatial structure from MRI into the image reconstruction by using optical data (7). This is done through a

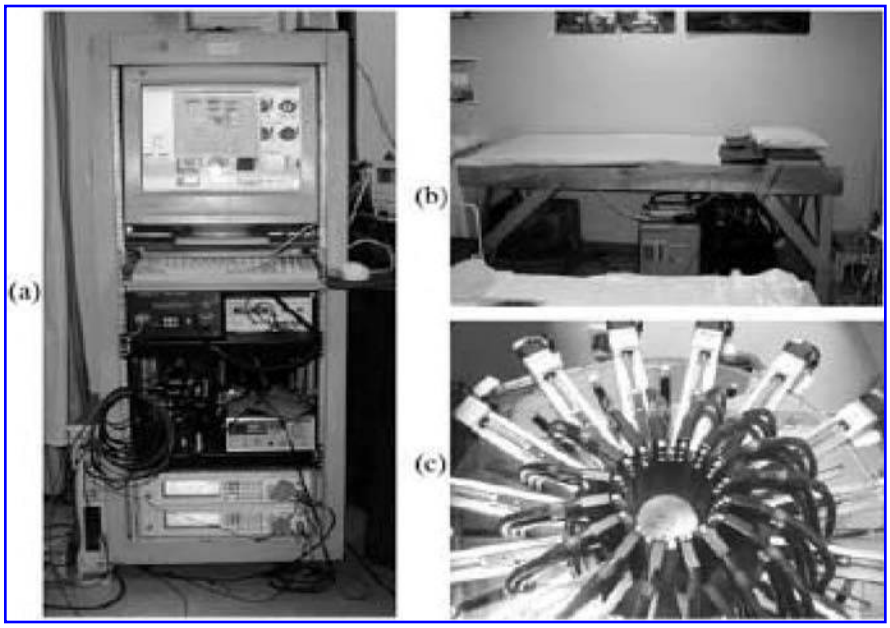

FIG. 1. (a) Photograph of the stand-alone NIR tomography system computer and light generation and detection modules. As shown in (**b**), the patient lies prone on this examination table with breast pendant through an opening. Underneath the bed, (**c**) the motorized fiber optic array is brought into contact with the breast.

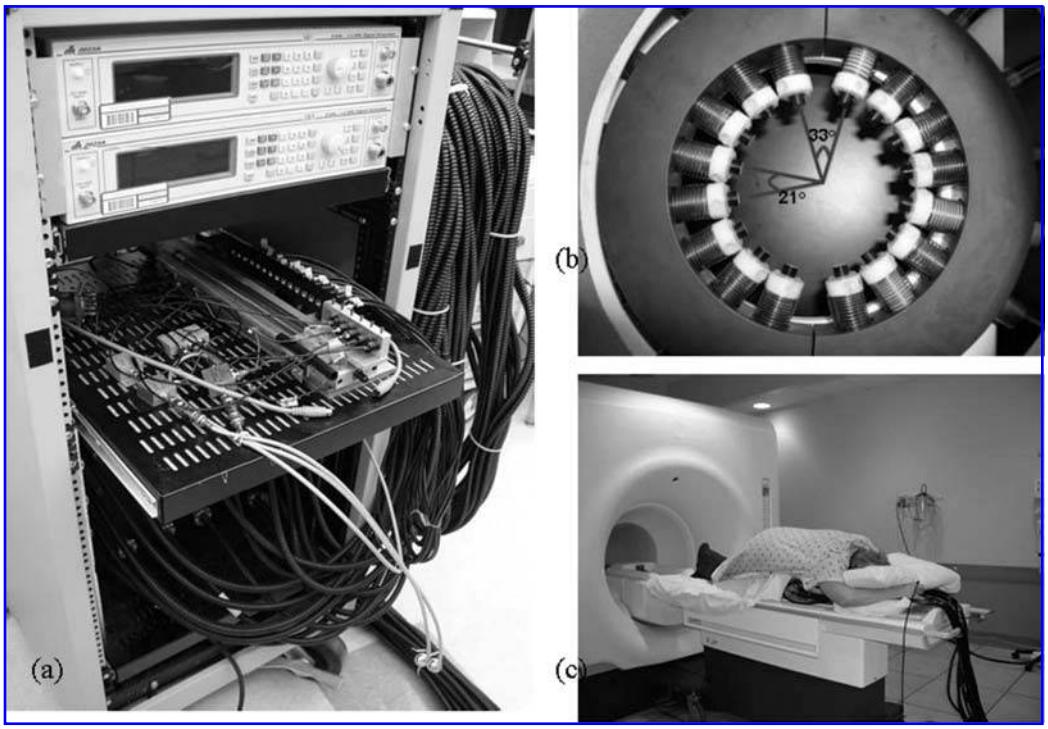

FIG. 2. A photograph of our portable MRI–NIR computer-controlled tomography system is shown (a) with the frequency generators, the linear-translation optical-switching stage, the PMT detection plate, and 13-m bifurcated optical fiber bundles coiled on the side of the cart. An open architecture breast-array coil (**b**) houses the NIR fiber array positioning system, which can be adjusted to fit the pendant breast. The patient lies prone (**c**) on the MRI platform with breast pendant through hole.

laplacian-type operator that uses the MRI spatial structure and boundaries between tissue types to guide the optical image reconstruction. The image reconstruction solves an inverse problem where the spatial maps of the chromophore concentrations and scatter parameters are obtained based on the periphery measurements of amplitude and phase of light fluence. The use of priors limits the solution space of this inverse problem, making it robust, and increases the spatial resolution of the functional images to that of the T_1-weighted images; our studies (10) have shown that implementation of these priors is the key to obtaining quantitatively accurate functional images from optical measurements. The chart in Fig. 3 shows the steps involved in obtaining images from the MR-guided optical tomography system. In this article, 2-D images have been displayed and analyzed, but 3-D image reconstruction also is feasible by using the same measurements.

Human subjects

The Dartmouth Internal Review Board approved the clinical study protocol for all subjects imaged in both systems, and informed consent was obtained from the volunteers before the examination. The study included imaging normal volunteers (without any mammographically detected abnormality) as well as volunteers with abnormalities at the Dartmouth Hitchcock Medical Center. For all subjects, the approximate plane of tumor was marked before the examination by a radiologist (S.P.), so that the optical data could be obtained in the plane or as close to it as possible. For normal subjects, the plane was defined in a similar manner, just with a mock plane defined to image in. During the examinations, a registered nurse guided the subject onto the imaging table, placing the breast through the hole and adjusting for optimal positioning of the optical fibers into the plane of the suspected abnormality. The contact of the optical fibers was achieved based on subject comfort and use of pressure sensors so that mild compression was limited to contact of all fibers. After imaging, all abnormal mammograms were interpreted to again specify the malignancy and location, and pathology studies were completed on the excised tumor tissues, giving information regarding the tumor histologic type, grade, and size.

RESULTS

These results have been classified into two sections: Section I shows results obtained using the stand-alone NIR tomography system, and Section II shows results of using the hybrid MR-NIR tomography system. Data obtained from experiments and clinical studies are shown, comprising measurements from both healthy volunteers and volunteers with abnormalities. The data are presented in a somewhat historical order, showing the capabilities and limitations of quantifying oxygen saturation first, without MRI guidance, whereas diffuse tomography is used to recover low-resolution images. Then in the second half of the results, the MRI-guided images and data of NIR tomography are presented and interpreted.

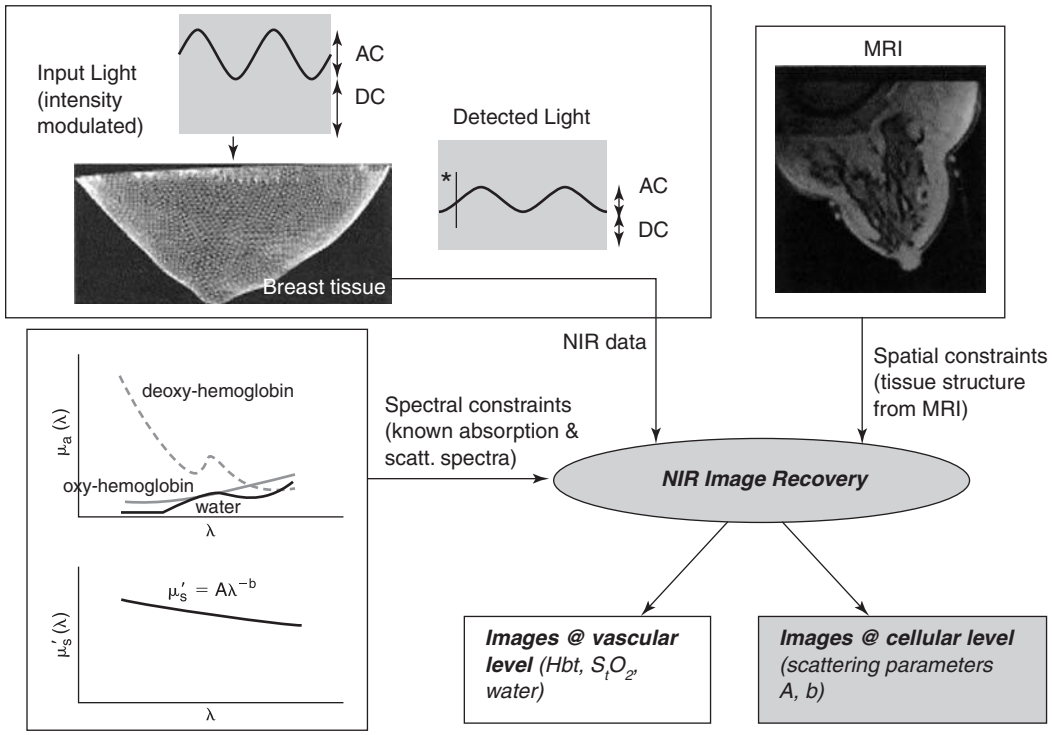

FIG. 3. Flowchart showing the approach to multimodality MR-guided optical imaging. Optical measurements of amplitude and phase are obtained from the periphery of the breast after shining light through lasers at six different wavelengths, in parallel with the MR examination. The MRI is used to create patient-specific meshes with prior knowledge of tissue boundaries (adipose, glandular, and tumor areas) and by using these spatial priors along with spectral constraints, images of total hemoglobin, oxygen saturation, water, and scatter are obtained.

Section I: Using stand-alone NIR tomography system

Oxygen dissociation curve. In malignancies, the pO_2 values are presumed to be <20 mm Hg, although this clearly depends on the tissue type and lesion size (77). However, this is an important parameter for oxygen-saturation imaging, because the oxygen itself is not imaged, but the spectral changes in hemoglobin due to the binding status with oxygen, and additionally, the hemoglobin is predominantly confined to the vascular space where the oxygenation level is highest. Because the oxygen saturation of the tissue is related to the partial pressure of oxygen in the tissue by the Hill or oxygen-dissociation curve, measurement of the Hill curve can give a good idea of the sensitivity of the imaging system to low pO_2 values. To characterize this curve for the system, data were acquired by using a phantom solution containing 1% whole blood and 1% Intralipid in saline, in a thin-walled plastic container, 70 mm in diameter. Intralipid is a commercially produced medicinal nutrition supplement that has well-characterized sizes and scattering parameters and is commonly used throughout NIR studies to simulate the scattering properties of soft mammalian tissues (54). The 1% whole blood was found to have 18 μM hemoglobin, and the oxygenation of the solution was reduced by varying the pO_2 values from 150 to 0 mm Hg by addition of yeast. The pO_2 was independently measured by using a chemical microelectrode, after calibration of the electrode overnight in saline solution. By varying the pO_2 gradually, with a small amount of yeast and making measurements over this period, the pO_2 eventually was reduced to zero, and a complete set of data over the required range was obtained. Measurements of this phantom at six wavelengths and image reconstruction gave Hb_T, S_tO_2, water, scatter amplitude, and scatter power images from which the mean and standard deviation have been plotted in Fig. 4a. The oxygen saturation in Fig. 4a follows the theoretical Hill curve (75) reasonably well, with a mean error of 7.7%, with the worst accuracy close to zero pO_2 (possibly due to noisier data, owing to high deoxyhemoglobin absorption at the lower wavelength, 661 nm) and considerably higher accuracy when it is >80% saturation. For pO_2 <20 mm Hg, oxygen saturation is still accurate to within 15%, with a low standard deviation in the images. Interestingly, in this type of imaging, although the accuracy could be off by 7–15%, the repeatability is exceptionally good, such that calibration approaches might be used to adjust from one level to another. However, addition of more wavelengths or better spatial localization of the interior regions is also well known to improve accuracy, as is studied later.

With variation of pO_2, the total apparent hemoglobin concentration stayed approximately constant (Fig. 4b), with a mean value of 17.5 ± 2.1 μM, which is within 97% of the true value given earlier, the water exhibited a mean value of 94.2 ± 8.3%. Both parameters showed some crosstalk at pO_2 values <11 mm Hg, which is possibly unavoidable because of the limited number of wavelengths used in these data (six total). The scatter

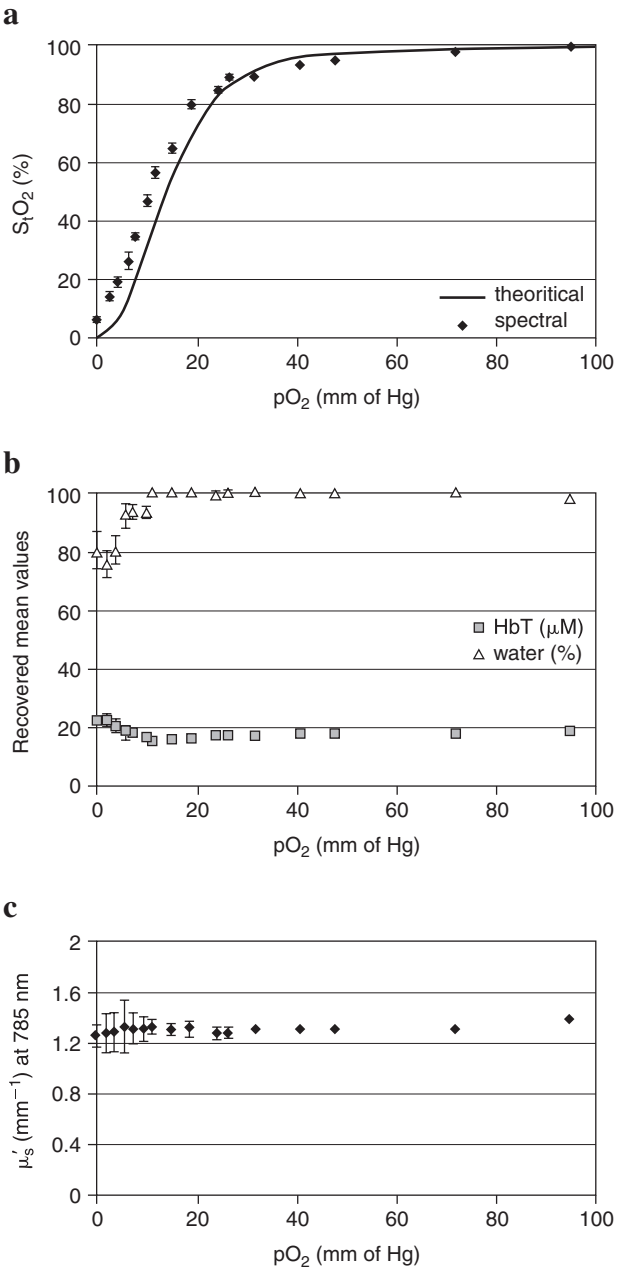

FIG. 4. Estimated mean values are shown from homogeneous reconstructions of a phantom with varying oxygen partial pressure (pO_2) of the solution, induced by addition of yeast. The oxygen saturation is shown in (**a**) along with a theoretic estimate calculated as the Hill curve. The total hemoglobin and percentage water are shown in (**b**), with the theoretically estimated values of 18 μM and 100%, respectively, and should not vary with changes in oxygenation. The reduced scattering coefficient at 785 nm is shown in (**c**) and is expected to stay constant.

parameters (not shown here), described by scatter amplitude and power (wavelength independent), stayed approximately constant until a pO_2 of 11 mm Hg, beyond which both show some variation, which could be the result of crosstalk between the two parameters. Above 11 mm Hg, scatter amplitude has value of 0.92 ± 0.04 when the wavelength is in microns, and scatter power has values 1.49 ± 0.14. The reduced scattering coefficient stayed constant throughout, as shown for 785 nm, in Fig. 4c, with a mean of 1.3 ± 0.03 per mm.

It is important to note that in addition to the Hill curve found here, changes in the solution pH or CO_2 concentration will affect the shape of this curve and the level of a few mm Hg change in the P50 point. The values used in the solution here were for saline solution, which is typical of the pH of many tissues, although within tumor tissues, the slightly higher acidity could shift this curve a few mm Hg at most.

Correlation of oxygen saturation with radiographic density. With measurements from 60 women imaged at the Dartmouth Hitchcock Medical Center under the protocol approved for healthy volunteers, the optical images for the left and right breasts were obtained. The demographic information and the average functional parameters relating to this population size are tabulated in Table 1. By using the x-ray mammograms of these subjects, they were classified into four categories given by BIRADS as (a) almost entirely fatty, (b) scattered fibroglandular, (c) heterogeneously dense, and (d) extremely dense. Optical data from each examination were calibrated and used to reconstruct for the functional images. Artifacts sometimes are found near the boundary; hence, the imaging field evaluated was reduced by 12% of the total breast diameter for each cross section to compute the breast average and SD. Each of the functional parameters was then tested for the ability to separate the radiodensity categories by using statistical analysis comprising a random coefficients regression model. Following previous results (59), possible correlation between the left and right breasts of an individual was taken into account in the statistical model. Some of these results were described in Srinivasan *et al.* (67, 68). This analysis showed that oxygen saturation could separate the heterogeneously and extremely dense breasts from predominantly fatty breasts with statistically significant p values of 0.038 and 0.035, respectively. Table 2 gives the coefficients and standard errors along with p values for each of the correlations tested for oxygen saturation. Figure 5 shows a box-plot of oxygen saturation for each of the density categories and illustrates the trend of reduced oxygenation with increasing density. Density of tissue is correlated to the fibroglandular volume fraction (81), and it is well known that cancers evolve from the glandular areas of tissue; this tissue is also more metabolically active when compared with adi-

TABLE 1. AVERAGE AND STANDARD DEVIATION FOR DEMOGAPHIC AND NIR PARAMETERS FROM 60 NORMAL SUBJECTS

Property	*Mean ± SD*	*Range*
BMI (kg/m^2)	25 ± 4	18–36
Age (yr)	57 ± 10.8	41–79
Breast diameter (mm)	80.6 ± 13.9	49–124
Hb_T (μM)	16.6 ± 4.6	6–31
S_tO_2 (%)	68.3 ± 7.2	46–96
Water (%)	51.5 ± 14.1	28–94
Scatt ampl	1.2 ± 0.25	0.59–2.2
Scatt power	0.7 ± 0.44	0.1–3

TABLE 2. RESULTS OF STATISTICAL ANALYSIS TESTING FOR SIGNIFICANT DIFFERENCES BETWEEN EACH OF THE RADIOGRAPHIC DENSITY CATEGORIES RELATIVE TO THE FATTY ONE, USING NIR PARAMETERS

NIR parameters	*Radio-density groups*	*Coefficient (SE)*	t *Test* p *value*
S_tO_2 (%)	Fatty	Used as the reference	
	Scattered	−2.32 (2.23)	0.3
	Het. dense	−5.00 (2.38)	0.038
	Extr. dense	−6.89 (3.23)	0.035

pose tissue; thus, it seems reasonable that the average oxygen saturation might be lower in these more-active tissues because of the higher oxygen extraction fraction.

Results from a volunteer with an infiltrating ductal carcinoma. By using measurements from a 73-year-old female volunteer diagnosed with infiltrating ductal carcinoma, optical functional images were obtained as part of the study to investigate the potential of these images in diagnosis. Figure 6a shows a magnified close-up mediolateral view of the mammogram of the patient. The mammograms revealed a speculated mass of size 25 mm (maximum focal diameter) peripherally located at 2:30 clock-face position with architectural distortion over a larger area. A core-needle biopsy was used to diagnose the mass as an infiltrating ductal carcinoma with lobular features. The NIR measurements were obtained 2 weeks after the biopsy and by using spectral image reconstruction, the functional images were obtained and are shown in Fig. 6b, excluding scatter. The breast diameter corresponding to the plane of measurement was 104 mm, and the subject had a heterogeneously dense breast.

The tumor is clearly visible as a localized increase at the right side of the images, close to 2 o'clock position, in all of the NIR images. Total hemoglobin shows nearly 2:1 contrast in tumor versus background. Oxygen saturation shows a reduction in the tumor region, indicative of a potential hypoxic situation. The ability to image hypovascular or hypoxic areas of the tumor has repercussion in predicting radiotreatment response, yet has not been extensively tested with NIR imaging (49). An increase in water content as well as in scatter was also observed. The av-

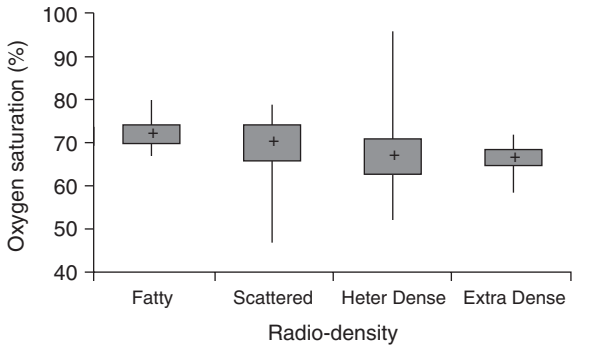

FIG. 5. The box plot of oxygen saturation from 60 mammographically healthy volunteers categorized into four radiographic density categories as fatty, scattered, heterogeneously dense, and extremely dense, based on their mammograms. Oxygen-saturation values are significantly different between heterogeneously dense and extremely dense tissue relative to the adipose with p values of 0.038 and 0.035, respectively, perhaps reflecting differences in the supply and demand in fibroglandular tissues relative to fatty tissues.

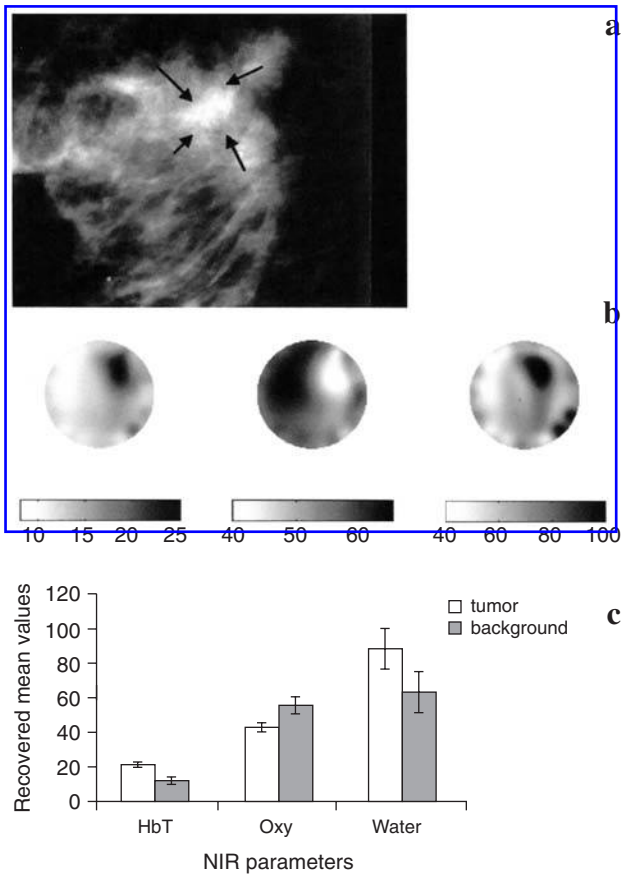

FIG. 6. (a) Left magnified close-up mediolateral mammogram from the left breast from a 73-year-old woman with a 2.5-cm spiculated mass (black arrows) diagnosed as infiltrating ductal carcinoma by core-needle biopsy. (**b**) Images for Hb_T (μM), S_tO_2 (%), and water (%) obtained from NIR tomography system. Images correspond well with tumor location (given as 2:30 clock-face position, close to the periphery) from the mammogram, where the total breast diameter in these images was 88 mm. (**c**) The average total hemoglobin, oxygen saturation, and water in tumor and background. Total hemoglobin in the tumor exhibits an increase relative to the background, whereas oxygen saturation is reduced along with an increase.

erage and standard deviation of Hb_T, S_tO_2, and water in the tumor region (defined by a region within the full-width half maximum of the peak value) and the background are shown in Fig. 6c and are indicative of the quantitative differences observable through the functional parameters. Oxygen saturation, in particular, was reduced from an average of 56.4% in the background to 43.6% in the tumor.

Section II: Using MR-guided NIR tomography system

Representative images from healthy volunteers without clinically detected abnormalities. As part of the Dartmouth protocol to study healthy volunteers (without clinically detected abnormality) in the hybrid MR-guided optical system, 11 volunteers have been imaged to date. For each patient, the optical measurements were obtained in parallel with the MR examination, and the MR images were used to guide the image reconstruction, as described earlier. This ensures the resolution of MR as well as the functional aspect of NIR imaging. A 2-D mesh was created for the plane of optical measurement, by segmentation of the MR for the corresponding plane, with tags for fibroglandular and adipose regions. The calibrated data were then used along with this mesh for reconstructing the functional images; some representative images for total hemoglobin, oxygen saturation, water content, and scatter are shown in Fig. 7 for six of these patients. No particular trend is visible in oxygen saturation in these images. The main features in general are an increase in total hemoglobin, water, and scatter power in the fibroglandular areas compared with the adipose regions. Oxygenation either stays approximately homogeneous or shows a reduction in the denser tissue regions compared with adipose areas. The average values for each of these parameters, with standard deviation obtained from the images, was analyzed for statistical correlations with tissue types and presented in Brooksby *et al*. (9). An interesting correlation that surfaced is that the percentage of adipose tissue in the breast correlated with the adipose-tissue oxygen saturation ($p = 0.027$ for slope significantly different from zero). Figure 8 shows this correlation graphically. The segmented MRI in the NIR imaging plane provided estimates of the adipose tissue by area, which could possibly be related to body mass index. For these 11subjects, the percentage adipose tissue by area ranged from 49 to 86, with an average of 70. A paired t test confirmed that subjects with scattered radiographic density had a higher percentage adipose content than did those with heterogeneously dense, or extremely dense breast tissue ($r = 0.30$; $p < 0.001$). This correlates well with Fig. 5, obtained from data by using the stand-alone NIR system, showing the reduced oxygen saturation in the higher breast-density categories. The NIR signatures responsible for both graphs are

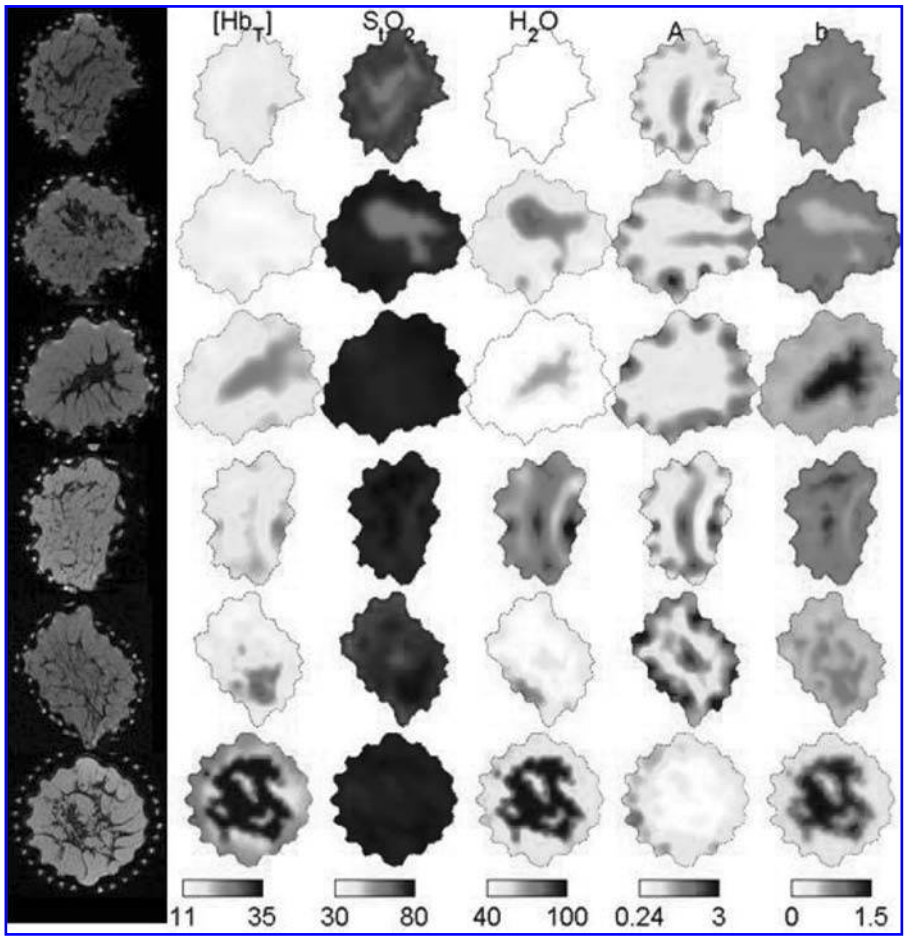

FIG. 7. Oblique coronal T_1-weighted gradient-echo MR images for six mammographically healthy volunteers, which are then followed by the corresponding NIR images of total hemoglobin (μM), oxygen saturation (%), water (%), scatter amplitude, and power. The general trend is increased total hemoglobin, water, and scatter power in the fibroglandular areas (dark in the MRI) as compared to the adipose areas (lighter color in the MRI).

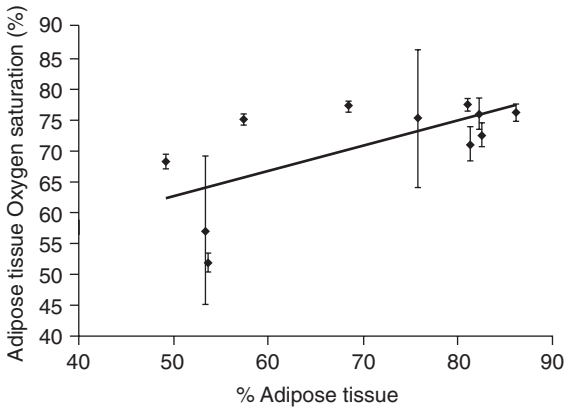

FIG. 8. The average of oxygen saturation in the adipose tissue region is plotted against the percentage adipose tissue by area (calculated from the MR images) from 11 mammographically healthy subjects, imaged in the hybrid MR-guided optical system. The oxygen saturation is correlated with the percentage of adipose tissue, with a p value of 0.027 for the probability that the slope is different from zero.

essentially the same: the sampling of the spectra of oxy- and deoxyhemoglobin. These estimates were expected to become more accurate with increasing prior knowledge, in this case from MRI, as the accuracy of the data is improved with the superior localization of the different tissue types.

Results from volunteer with infiltrating ductal carcinoma. One case report of a 29-year-old volunteer who underwent the MR-NIR examination is shown here. She was diagnosed through a mastectomy, after undergoing neoadjuvant chemotherapy, as having a 20-mm infiltrating ductal carcinoma in the breast. The MRI was used to segment the fibroglandular and adipose areas of the breast and create a 2-D mesh, and a contrast-enhanced MRI was used to provide tumor location in the mesh. By using measurements from the NIR system obtained concurrent with the MRI, and after suitable calibration, image reconstruction was carried out by using the patient-specific mesh. Figure 9a shows the contrast MRI followed by the optical images in Fig. 9b–d for total hemoglobin, oxygen saturation, and water. Consistent with the trend found in the malignancy studied in the previous case study, this subject also showed an increase in total hemoglobin, water, and scatter in the location of the tumor, along with a decrease in oxygen saturation in the tumor. Consistent with the trend observed in the healthy volunteers, the fibroglandular region shows higher total hemoglobin and slightly reduced oxygenation, when compared with the adipose tissue regions. Some artifacts are observable in the water images close to the outer boundary, possibly because of hypersensitivity of the measurements to changes in this area. The MRI showed some necrosis in the slice right below the imaging plane, and this is possibly captured in the oxygen-saturation image as a reduction.

DISCUSSION

Whereas NIR spectroscopy to quantify oxygen saturation has had a long history over the past three decades (36), a productive level of success the ability to image oxygen saturation quantitatively with high accuracy has remained somewhat elusive. Recent data in breast imaging shows excellent potential (17, 60), yet a need exists to use more wavelengths and combine the approach with standard imaging technologies. Much of the work discussed here has been focused on the use of NIR as a low-cost add-on to MRI. This approach has the potential to image millimeter-scale tumors along with their functional characterization. Clearly, resolution depends on how much of the MR information is incorporated into the optical images, through the meshing and the algorithm for implementing the prior structural information. Currently, effort is under way to increase the resolution of the meshes and move toward fully automated 3-D imaging capabilities. The priors have been implemented in a manner that they merely guide the image reconstruction so that no hard constraints are imposed on the functional parameter recovery itself. This ensures reconstruction of false-positives as well as false-negatives from MRI, in the optical images.

Both the stand-alone NIR system and the hybrid MR-NIR system have been calibrated through several experiments involving tissue-simulating phantoms (11, 66). The use of blood and Intralipid, along with agents like gelatin, have mimicked the constituents of the breast and its stiffness so that the spectral features could be accurately reproduced (54). Although the results were specific to the phantom types and complexity, as well as size of inclusions, for a tumor size of 8 mm and larger, the expected error in quantification is 15% and lower with the

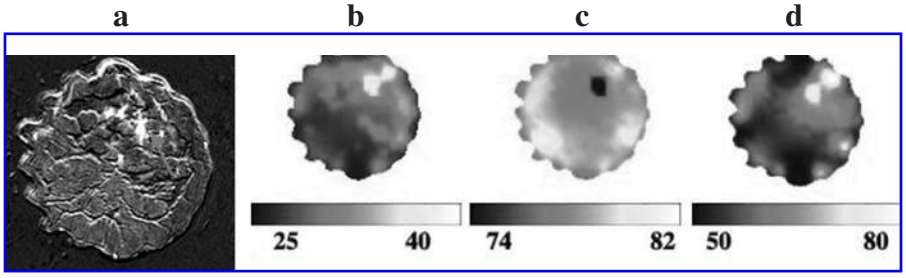

FIG. 9. (a) The contrast-enhanced MR image shows the location of the tumor in the breast of a 29-year-old volunteer. The tumor was diagnosed as a 20-mm infiltrating ductal carcinoma and imaged with the hybrid MR-guided NIR system. The corresponding images of total hemoglobin (μM), oxygen saturation (%), and water (%) are shown in **b–d**. Total hemoglobin and water show an increase in the area of the tumor. The MR also revealed areas of necrotic tissue in the tumor, possibly reflected in the reduction in oxygen saturation in the tumor location.

stand-alone system (4, 58). This accuracy is expected to increase with the use of spectral priors (69) and to be extended to smaller sizes with the MRI information. The range of the average values for the NIR parameters measured by using clinical data from healthy volunteers with both the optical systems is also consistent with values from the literature (15, 24).

The results of using experimental data mimicking hypoxia of tissue through slow deoxygenation of a blood–Intralipid sample indicate the ability of optical tomography to image low-oxygenation conditions. The average error in recovering oxygen saturation was 7.7% mean error, with worst accuracy close to zero pO_2: even <20 mm Hg, oxygen saturation was obtained with $<15\%$ mean error. As expected, total hemoglobin, water, and scatter stayed constant with this change in oxygenation, indicating that we could monitor pO_2 changes without significant crosstalk between the parameters. Indeed, the experiment was carried out by using a homogeneous phantom, and the accuracy may be reduced somewhat when extended to heterogeneities. We have simulated hypoxic conditions in simulations with noise and found results for all functional parameters accurate with an average error of 15%, for up to 5% noise in measurements (65). Unfortunately the largest errors in predicting oxygen saturation are at the lower end of the oxygenation values, where the pO_2 values are <10 mm Hg. This is unfortunate, as this range is where the most relevant information would be about malignant tumors; however, the ability to obtain truly accurate values is probably less important than the ability to obtain reliable relative values. Still, quantitative interpretation of SO_2 values in terms of radiologically hypoxic areas of tissue may be difficult if not unreliable with the current technology. Improvements in adding more wavelengths to the spectroscopy system have been shown clearly to increase the accuracy of predicting oxygen saturation at these lower values.

In the two case studies involving imaging volunteers with cancers, oxygen saturation decreased in both malignancies at the location of the tumor compared with the surrounding tissue, agreeing with predictions of hypoxia in cancers. Additionally, the MRI of the second subject imaged in the hybrid system revealed areas of necrosis in the tumor, which was likely reflected in the oxygen saturation. The hybrid system of NIR add-on to MRI allows visualization of this change at a much higher resolution than the stand-alone NIR system, providing accurate delineation of hypoxic tissue segments.

In results presented earlier, oxygen saturation could separate heterogeneously dense and extremely dense tissue from adipose tissue with statistically significant p values of 0.038 and 0.035, respectively. The occurrence and risk of cancers is higher in mammographically dense breasts (2, 73); clearly some aspect of the dense tissue results in the growth of carcinogens in the epithelium for the women in whom cancer is developing (73). Thus, radiographic density may be thought of as a marker of the metabolic activity of the breast: the denser the breast, the more metabolically active and higher the risk of cancer. Scattering measured by using NIR systems has already been shown to be a noninvasive risk predictor (3, 62); oxygen saturation may provide yet another surrogate measure of this risk factor. In addition, breast density and rapid tumor growth are primarily responsible for decreased mammographic sensitivity in younger women (13), and oxygen saturation can address both of these issues.

Oxygen saturation also reduced with decreasing percentage of adipose tissue as imaged by the hybrid MR-NIR system, again reinforcing this conclusion, because adipose tissue percentage is inversely related to radiographic density. The adipose tissue fraction varies with factors such as age and body mass index.

CONCLUSIONS

Understanding healthy and diseased tissues *in vivo* through a noninvasive mechanism is a powerful tool in medical diagnostics and imaging. The results presented here agree with observations from radiology and pathology, as relating to vascular trends with radiographic density in healthy breast tissue and hypoxia to malignancies. Combined with MRI, this dual-modality imaging yields millimeter resolution images relating to the vascular and molecular architecture of the breast and will potentially reduce the unnecessary biopsies to determine diagnosis in the future.

ACKNOWLEDGMENTS

We are grateful for the participation by Ben Brooksby, Ph.D., Hamid Dehghani, Ph.D., Christine Kogel, R.N., and John Weaver, Ph.D. in this research, and for funding provided by the National Cancer Institute through awards PO1CA80139 and R01CA069544.

ABBREVIATIONS

2-D, two-dimensional; 3-D, three-dimensional; BIRADS, breast imaging reporting and data system; MRI, magnetic resonance imaging; NIR, near infrared; SNR, signal-to-noise ratio.

REFERENCES

1. American College of Radiology. *Breast imaging reporting and data system (BIRADS)*. Reston, VA: American College of Radiology, 1998.
2. Barlow WE, White E, Ballart-Barbash R, Vacek PM, Titus-Ernstoff L, Carney PA, Tice JA, Buist DSM, Geller BM, Rosenberg R, Yankaskas BC, and Kerlikowske K. Prospective breast cancer risk prediction model for women undergoing screening mammography. *J Natl Cancer Inst* 98: 1204–1214, 2006.
3. Blyschak K, Simick M, Jong R, and Lilge L. Classification of breast tissue density by optical transillumination spectroscopy: optical and physiological effects governing predictive value. *Med Phys* 31: 1398–1414, 2004.
4. Boas DA, O'Leary MA, Chance B, and Yodh AG. Detection and characterization of optical inhomogeneities with diffuse photon density waves: a signal-to-noise analysis. *Appl Opt* 36: 75–92, 1997.
5. Boulnois J-L. Photophysical processes in recent medical laser developments: a review. *Lasers Med Sci* 1: 47–66, 1986.
6. Brizel DM, Scully SP, Harrelson JM, Layfield LJ, Bean JM, Prosnitz LR, and Dewhirst MW. Tumor oxygenation predicts for the

likelihood of distant metastases in human soft tissue sarcoma. *Cancer Res* 56: 941–943, 1996.
7. Brooksby B, Jiang S, Dehghani H, Pogue BW, Paulsen KD, Weaver J, Kogel C, and Poplack SP. Combining near infrared tomography and magnetic resonance imaging to study in vivo breast tissue: implementation of a laplacian-type regularization to incorporate MR structure. *J Biomed Opt* 10: 51504–51501, 2005.
8. Brooksby B, Jiang S, Dehghani H, Pogue BW, Paulsen KD, Weaver JB, Kogel C, and Poplack SP. Combining near infrared tomography and magnetic resonance imaging to study in vivo breast tissue: implementation of a laplacian-type regularization to incorporate MR structure. *J Biomed Opt* 10: 051504–051510, 2005.
9. Brooksby B, Pogue BW, Jiang S, Dehghani H, Srinivasan S, Kogel C, Weaver J, Poplack SP, and Paulsen KD. Imaging breast adipose and fibroglandular tissue molecular signatures using hybrid MRI-guided near-infrared spectral tomography. *Proc Natl Acad Sci U S A* 103: 8828–8833, 2006.
10. Brooksby B, Srinivasan S, Jiang S, Dehghani H, Pogue BW, and Paulsen KD. Spectral-prior information improves near-infrared diffuse tomography more than spatial-prior. *Optics Lett* 30: 1968–1970, 2005.
11. Brooksby BA, Jiang S, Dehghani H, Kogel C, Doyley M, Weaver JB, Poplack SP, Pogue BW, and Paulsen KD. Magnetic resonance-guided near-infrared tomography of the breast. *Rev Sci Instr* 75: 5262–5270, 2004.
12. Brown DW, Picot PA, Naeini JG, Springett R, Delpy DT, and Lee TY. Quantitative near infrared spectroscopy measurement of cerebral hemodynamics in newborn piglets. *Pediatr Res* 51: 564–570, 2002.
13. Buist DSM, Porter PL, Lehman C, Taplin SH, and White E. Factors contributing to mammography failure in women aged 40-49 years. *J Natl Cancer Inst* 96: 1432–1440, 2004.
14. Cerretelli P and Binzoni T. The contribution of NMR, NIRS and their combination to the functional assessment of human muscle. *Int J Sports Med* 18: S270–S279, 1997.
15. Cerussi A, Jakubowski D, Shah N, Bevilacqua F, Lanning R, Berger AJ, Hsiang D, Butler J, Holcombe RF, and Tromberg BJ. Spectroscopy enhances the information content of optical mammography. *J Biomed Opt* 7: 60–71, 2002.
16. Cerussi A, Shah N, Hsiang D, Durkin A, Butler J, and Tromberg B. In vivo absorption, scattering, and physiologic properties of 58 malignant breast tumors determined by broadband diffuse optical spectroscopy. *J Biomed Opt* 11: 044005–044016, 2006.
17. Chance B, Nioka S, Zhang J, Conant EF, Hwang E, Briest S, Orel SG, and Czerniecki BJ. Breast cancer detection based on incremental biochemical and physiological properties of breast cancers: a six-year, two-site study. *Acad Radiol* 12: 925–933, 2005.
18. Chance B, Nioka S, Zhang J, Conant EF, Hwang E, Briest S, Orel SG, Schnall MD, and Czerniecki BJ. Breast cancer detection based on incremental biochemical and physiological properties of breast cancers: a six-year, two-site study. *Acad Radiol* 12: 925–933, 2005.
19. Chance B, Nioka S, Kent J, McCully K, Fountain M, Greenfield R, Holtom G. Time-resolved spectroscopy of hemoglobin and myoglobin in resting and ischemic muscle. *Analyt Biochem* 174: 698–707, 1988.
20. Choe R, Corlu A, Lee K, Durduran T, Konecky SD, Grosicka-Koptyra M, Arridge SR, Czerniecki BJ, Fraker DL, DeMichele A, Chance B, Rosen MA, and Yodh AG. Diffuse optical tomography of breast cancer during neoadjuvant chemotherapy: a case study with comparison to MRI. *Med Phys* 32: 1128–1139, 2005.
21. Corlu A, Choe R, Durduran T, Lee K, Schweiger M, Arridge SR, Hillman EM, and Yodh AG. Diffuse optical tomography with spectral constraints and wavelength optimization. *Appl Opt* 44: 2082–2093, 2005.
22. Dehghani H, Pogue BW, Poplack SP, and Paulsen KD. Multi-wavelength three-dimensional near-infrared tomography of the breast: initial simulation, phantom, and clinical results. *Appl Opt* 42: 135–145, 2003.
23. Dewhirst MW, Klitzman B, Braun RD, Brizel DM, Haroon ZA, and Secomb TW. Review of methods used to study oxygen transport at the microcirculatory level. *Int J Cancer* 90: 237–255, 2000.
24. Durduran T, Choe R, Culver JP, Zubkov L, Holboke MJ, Giammarco J, Chance B, and Yodh AJ. Bulk optical properties of healthy female breast tissue. *Phys Med Biol* 47: 2847–2861, 2002.
25. Elmore JG, Barton MB, Moceri VM, Polk S, Arena PJ, and Fletcher SW. Ten-year risk of false positive screening mammograms and clinical breast examinations. *N Engl J Med* 338: 1089–1096, 1998.
26. Gilles R, Guinebretiere JM, Lucidarme O, Cluzel P, Janaud G, Finet JF, Tardivon A, Masselot J, and Vanel D. Nonpalpable breast tumors: diagnosis with contrast-enhanced subtraction dynamic MR imaging. *Radiology* 191: 625–631, 1994.
27. Gratton E, Fantini S, Franceschini MA, Gratton G, and Fabiani M. Measurements of scattering and absorption changes in muscle and brain. *Phil Trans R Soc Lond B* 352: 727–735, 1997.
28. Gribbestad IS, Nilsen G, Fjosne H, Fougner R, Haugen OA, Petersen SB, Rinck PA, and Kvinnsland S. Contrast-enhanced magnetic resonance imaging of the breast. *Acta Oncol* 31: 833–842, 1992.
29. Grosenick D, Wabnitz H, Moesta KT, Mucke J, Schlag PM, and Rinneberg H. Time-domain scanning optical mammography, II: optical properties and tissue parameters of 87 carcinomas. *Phys Med Biol* 50: 2451–2468, 2005.
30. Hebden JC, Gibson A, Yusof RM, Everdell N, Hillman EM, Delpy DT, Arridge SR, Austin T, Meek JH, and Wyatt JS. Three-dimensional optical tomography of the premature infant brain. *Phys Med Biol* 47: 4155–4166, 2002.
31. Hockel M and Vaupel P. Tumor hypoxia: definitions and current clinical, biologic, and molecular aspects. *J Natl Cancer Inst* 93: 266–276, 2001.
32. Hueber DM, Franceschini MA, Ma HY, Zhang Q, Ballesteros JR, Fantini S, Wallace D, Ntziachristos V, and Chance B. Non-invasive and quantitative near-infrared haemoglobin spectrometry in the piglet brain during hypoxic stress, using a frequency-domain multidistance instrument. *Phys Med Biol* 46: 41–62, 2001.
33. Hunter RJ, Patterson MS, Farrell TJ, and Hayward JE. Haemoglobin oxygenation of a two-layer tissue-simulating phantom from time-resolved reflectance: effect of top layer thickness. *Phys Med Biol* 47: 193–208, 2002.
34. Intes X, Djeziri S, Ichalalene Z, Mincu N, Wang Y, St-Jean P, Lesage F, Hall D, Boas D, Polyzos M, Fleiszer P, and Mesurolle B. Time-domain optical mammography softscan: initial results. *Acad Radiol* 12: 934–947, 2005.
35. Jakubowski DB, Cerussi AE, Bevilacqua F, Shah N, Hsiang D, Butler J, and Tromberg BJ. Monitoring neoadjuvant chemotherapy in breast cancer using quantitative diffuse optical spectroscopy: a case study. *J Biomed Opt* 9: 230–238, 2004.
36. Jobsis FF. Non-invasive, infra-red monitoring of cerebral and myocardial oxygen sufficiency and circulatory parameters. *Science* 198: 1264–1267, 1977.
37. Kienle A and Glanzmann T. In vivo determination of the optical properties of muscle with time-resolved reflectance using a layered model. *Phys Med Biol* 44: 2689–2702, 1999.
38. Kriege M, Brekelmans CT, Boetes C, Besnard PE, Zonderland HM, Obdeijn IM, Manoliu RA, Kok T, Peterse H, Tilanus-Linthorst MM, Muller SH, Meijer S, Oosterwijk JC, Beex LV, Tollenaar RA, de Koning HJ, Rutgers EJ, and Klijn JG. Efficacy of MRI and mammography for breast-cancer screening in women with a familial or genetic predisposition. *N Engl J Med* 351: 427–437, 2004.
39. Kuhl CK, Kuhn W, and Schild H. Management of women at high risk for breast cancer: new imaging beyond mammography. *Breast* 14: 480–486, 2005.
40. Kuszyk BS, Corl FM, Franano FN, Bluemke DA, Hofmann LV, Fortman BJ, and Fishman EK. Tumor transport physiology: implications for imaging and image-guided therapy. *AJR Am J Radiol* 177: 747–753, 2001.
41. Lehman CD, Blume JD, Weatherall P, Thickman D, Hylton N, Warner E, Pisano E, Schnitt SJ, Gatsonis C, Schnall M, DeAngelis GA, Stomper P, Rosen EL, O'Loughlin M, Harms S, and Bluemke DA. Screening women at high risk for breast cancer with mammography and magnetic resonance imaging. *Cancer* 103: 1898–1905, 2005.
42. McBride TO. Spectroscopic reconstructed near infrared tomo-

graphic imaging for breast cancer diagnosis. Thesis for Thayer School of Engineering, Dartmouth College, 2001, p. 200.
43. Mcbride TO, Pogue BW, Jiang S, Osterberg UL, and Paulsen KD. A parallel-detection frequency-domain near-infrared tomography system for hemoglobin imaging of the breast in vivo. *Rev Sci Instr* 72: 1817–1824, 2001.
44. McBride TO, Pogue BW, Jiang S, Osterberg UL, Paulsen KD, and Poplack SP. Initial studies of in vivo absorbing and scattering heterogeneity in near-infrared tomographic breast imaging. *Opt Lett* 26: 822–824, 2001.
45. Meglinski IV and Matcher SJ. Computer simulation of the skin reflectance spectra. *Comput Methods Programs Biomed* 70: 179–186, 2003.
46. Mourant JR, Fuselier T, Boyer J, Johnson TM, and Bigio IJ. Predictions and measurements of scattering and absorption over broad wavelength ranges in tissue phantoms. *Appl Opt* 36: 949–957, 1997.
47. Moyle JTB. *Pulse oximetry*. 2nd ed. BMJ Books, 2002.
48. Ntziachristos V, Yodh AG, Schnall MD, and Chance B. MRI-guided diffuse optical spectroscopy of malignant and benign breast lesions. *Neoplasia* 4: 347–354, 2002.
49. Okunieff P, Hoeckel M, Dunphy EP, Schlenger K, Knoop C, and Vaupel P. Oxygen tension distributions are sufficient to explain the local response of human breast tumors treated with radiation alone. *Int J Radiat Oncol Biol Phys* 26: 631–636, 1993.
50. Orel SG and Schnall MD. MR imaging of the breast for the detection, diagnosis, and staging of breast cancer. *Radiology* 220: 13–30, 2001.
51. Orel SG, Schnall MD, LiVolsi VA, and Troupin RH. Suspicious breast lesions: MR imaging with radiologic-pathologic correlation. *Radiology* 190: 485–493, 1994.
52. Paulsen KD and Jiang H. Spatially varying optical property reconstruction using a finite element diffusion equation approximation. *Med Phys* 22: 691–701, 1995.
53. Pogue BW, Jiang S, Dehghani H, Kogel C, Soho S, Srinivasan S, Song X, Poplack SP, and Paulsen KD. Characterization of hemoglobin, water and NIR scattering in breast tissue: analysis of intersubject variability and menstrual cycle changes relative to lesions. *J Biomed Opt* 9: 541–552, 2004.
54. Pogue BW and Patterson MS. Review of tissue simulating phantoms for optical spectroscopy, imaging and dosimetry. *J Biomed Opt* 11: 041102: 1–16, 2006.
55. Pogue BW and Paulsen KD. High resolution near infrared tomographic imaging simulations of rat cranium using a priori MRI structural information. *Opt Lett* 23: 1716–1718, 1998.
56. Pogue BW, Poplack SP, McBride TO, Wells WA, Osterman KS, Osterberg UL, and Paulsen KD. Quantitative hemoglobin tomography with diffuse near-infrared spectroscopy: pilot results in the breast. *Radiology* 218: 261–266, 2001.
57. Pogue BW, Song X, Tosteson TD, McBride TO, Jiang S, and Paulsen KD. Statistical analysis of non-linearly reconstructed near-infrared tomographic images, Part I: theory and simulations. *IEEE Trans Med Imaging* 21: 755–763, 2002.
58. Pogue BW, Willscher C, McBride TO, Osterberg UL, and Paulsen KD. Contrast-detail analysis for detection and characterization with near-infrared diffuse tomography. *Med Physics* 27: 2693–2700, 2000.
59. Poplack SP, Paulsen KD, Hartov A, Meaney PM, Pogue BW, Tosteson TD, Grove MR, Soho SK, and Wells WA. Electromagnetic breast imaging: average tissue property values in women with negative clinical findings. *Radiology* 231: 571–80, 2004.
60. Poplack SP, Paulsen KD, Hartov A, Meaney PM, Pogue BW, Tosteson TD, Soho SK, and Wells WA. Electromagnetic breast imaging: pilot results in women with abnormal mammography. *Radiology* 243: 350–359, 2007.
61 Schweiger M and Arridge SR. Optical tomographic reconstruction in a complex head model using a priori region boundary information. *Phys Med Biol* 44: 2703–2721, 1999.
62. Simick MK, Jong R, Wilson B, and Lilge L. Non-ionizing near-infrared radiation transillumination spectroscopy for breast tissue density and assessment of breast cancer risk. *J Biomed Opt* 9: 794–803, 2004.
63. Song X, Pogue BW, Tosteson TD, McBride TO, Jiang S, and Paulsen KD. Statistical analysis of non-linearly reconstructed near-infrared tomographic images, Part II: experimental studies. *IEEE Trans Med Imaging* 21: 764–772, 2002.
64. Spinelli L, Torricelli A, Pifferi A, Taroni P, Danesini GM, and Cubeddu R. Characterization of female breast lesions from multi-wavelength time-resolved optical mammography. *Phys Med Biol* 50: 2489–2502, 2005.
65. Srinivasan S. Spectroscopy-based quantification of chromophores and scattering in near infrared tomography. Thayer School of Engineering, Dartmouth College, p. 211, 2005.
66. Srinivasan S, Pogue BW, Brooksby B, Jiang S, Dehghani H, Kogel C, Wells WA, Poplack SP, and Paulsen KD. Near-infrared characterization of breast tumors in-vivo using spectrally-constrained reconstruction. *Tech Cancer Res Treat* 4: 513–526, 2005.
67. Srinivasan S, Pogue BW, Jiang S, Dehghani H, Kogel C, Soho S, Gibson JJ, Tosteson TD, Poplack SP, and Paulsen KD. In vivo hemoglobin and water concentration, oxygen saturation, and scattering estimates from near-infrared breast tomography using spectral reconstruction. *Acad Radiol* 13: 195–202, 2006.
68. Srinivasan S, Pogue BW, Jiang S, Dehghani H, Kogel C, Soho S, Gibson JJ, Tosteson TD, Poplack SP, and Paulsen KD. Interpreting hemoglobin and water concentration, oxygen saturation and scattering measured in vivo by near-infrared breast tomography. *Proc Natl Acad Sci U S A* 100: 12349–12354, 2003.
69. Srinivasan S, Pogue, BW, Jiang S, Dehghani H, and Paulsen, KD. Spectrally constrained chromophore and scattering NIR tomography provides quantitative and robust reconstruction. *Appl Opt* 44: 1858–1869, 2005.
70. Strangman G, Boas DA, and Sutton JP. Non-invasive neuroimaging using near-infrared light. *Biol Psychiatry* 52: 679–693, 2002.
71. Szmedra L, Im J, Nioka S, Chance B, and Rundell KW. Hemoglobin/myoglobin oxygen desaturation during Alpine skiing. *Med Sci Sports Exerc* 33: 232–236, 2001.
72. Tromberg BJ, Shah N, Lanning R, Cerussi A, Espinoza J, Pham T, Svaasand L, and Butler J. Non-invasive in vivo characterization of breast tumors using photon migration spectroscopy. *Neoplasia* (New York) 2: 26–40, 2000.
73. Ursin G, Hovanessian-Larsen L, Parisky YR, Pike MC, and Wu AH. Greatly increased occurrence of breast cancers in areas of mammographically dense tissue. *Breast Cancer Res* 7: R605–R608, 2005.
74. van Staveren HJ, Moes CJM, van Marle J, Prahl SA, and van Gemert MJC. Light scattering in Intralipid-10% in the wavelength range of 400-1100 nm. *Appl Opt* 30: 4507–4514, 1991.
75. Varjavand N. The interactive oxyhemoglobin dissociation curve. *http://www.ventworld.com/resources/oxydisso/dissoc.html*, 2002.
76. Vaupel P. Oxygen transport in tumors: characteristics and clinical implications. *Adv Exp Med Biol* 388: 341–351, 1996.
77. Vaupel P, Kallinowski F, and Okuneiff P. Blood flow, oxygen and nutrient supply, and metabolic microenvironment of human tumors: a review. *Cancer Res* 49: 6449–6465, 1989.
78. Vaupel P, Mayer A, Briest S, and Hockel M. Oxygenation gain factor: a novel parameter characterizing the association between hemoglobin level and the oxygenation status of breast cancers. *Cancer Res* 63: 7634–7637, 2003.
79. Wang X, Pogue BW, Jiang S, Dehghani H, Song X, Srinivasan S, Brooksby BA, Paulsen KD, Kogel C, Poplack AP, and Wells WA. Image reconstruction of effective Mie scattering parameters of breast tissue in vivo with near-infrared tomography. *J Biomed Opt* 11: 041106: 1–13, 2006.
80. Wang X, Pogue BW, Jiang S, Song X, Paulsen KD, Kogel C, Poplack SP, and Wells WA. Approximation of Mie scattering parameters from near-infrared tomography of health breast tissue in vivo. *J Biomed Opt* 10: 051704: 1–8, 2005.
81. Wei J, Chan HP, Helvie MA, Roubidoux MA, Sahiner B, Hadjiiski LM, Zhou C, Paquerault S, Chenevert T, and Goodsitt MM. Correlation between mammographic density and volumetric fibroglandular tissue estimated on breast MR images. *Med Phys* 31: 933–942, 2004.

82. Xu H, Dehghani H, Pogue BW, Springett R, Paulsen KD, and Dunn JF. Near-infrared imaging in the small animal brain: optimization of fiber positions. *J Biomed Opt* 8: 102–110, 2003.
83. Xu H, Pogue B, Springett R, and Dehghani H. Spectral derivative based image reconstruction provides inherent insensitivity to coupling and geometric errors. *Opt Lett* 30: 2912–2914, 2005.
84. Xu H, Springett R, Dehghani H, Pogue BW, Paulsen KD, and Dunn JF. Magnetic-resonance-imaging–coupled broadband near-infrared tomography system for small animal brain studies. *Appl Opt* 44: 2177–2188, 2005.
85. Yang Y, Soyemi OO, Landry MR, and Soller BR. Influence of a fat layer on the near infrared spectra of human muscle: quantitative analysis based on two-layered Monte Carlo simulations and phantom experiments. *Opt Express* 13: 1570–1579, 2005.

Address reprint requests to:
Subhadra Srinivasan, PhD
8000 Cummings Hall
Dartmouth College
Hanover, NH 03755

E-mail: subha@dartmouth.edu

Date of first submission to ARS Central, March 7, 2007; date of final revised submission, March 7, 2007; date of acceptance, March 8, 2007.

This article has been cited by:

1. J. L. Colli, Z. Wang, N. Johnsen, L. Grossman, B. R. Lee. 2012. Clamping renal artery alone produces less ischemic damage compared to clamping renal artery and vein together in two animal models: near-infrared tissue oximetry and quantitation of 8-isoprostane levels. *International Urology and Nephrology* . [CrossRef]
2. Arthur A. Caire, Xavier Alvarez, Sarah Conley, Alton Sartor, Benjamin R. Lee. 2011. Near-infrared tissue oximetry and digital image analysis: quantification of renal ischaemia in real time during partial nephrectomy. *BJU International* no-no. [CrossRef]
3. ZHIQIU LI, SHUDONG JIANG, VENKATARAMANAN KRISHNASWAMY, SCOTT C. DAVIS, SUBHADRA SRINIVASAN, KEITH D. PAULSEN, BRIAN W. POGUE. 2011. MR-GUIDED PULSE OXIMETRY IMAGING OF BREAST IN VIVO. *Journal of Innovative Optical Health Sciences* **04**:02, 199-208. [CrossRef]
4. T Durduran, R Choe, W B Baker, A G Yodh. 2010. Diffuse optics for tissue monitoring and tomography. *Reports on Progress in Physics* **73**:7, 076701. [CrossRef]
5. Anqi Zhang, Daqing Piao, Charles F. Bunting, Brian W. Pogue. 2010. Photon diffusion in a homogeneous medium bounded externally or internally by an infinitely long circular cylindrical applicator I Steady-state theory. *Journal of the Optical Society of America A* **27**:3, 648. [CrossRef]
6. R.B. Schulz, A. Ale, A. Sarantopoulos, M. Freyer, E. Soehngen, M. Zientkowska, V. Ntziachristos. 2010. Hybrid System for Simultaneous Fluorescence and X-Ray Computed Tomography. *IEEE Transactions on Medical Imaging* **29**:2, 465-473. [CrossRef]
7. Judith C Sluimer, Mat J Daemen. 2009. Novel concepts in atherogenesis: angiogenesis and hypoxia in atherosclerosis. *The Journal of Pathology* **218**:1, 7-29. [CrossRef]
8. Yang Yu, Ning Liu, Angelo Sassaroli, Sergio Fantini. 2009. Near-infrared spectral imaging of the female breast for quantitative oximetry in optical mammography. *Applied Optics* **48**:10, D225. [CrossRef]
9. Regine Choe, Soren D. Konecky, Alper Corlu, Kijoon Lee, Turgut Durduran, David R. Busch, Saurav Pathak, Brian J. Czerniecki, Julia Tchou, Douglas L. Fraker, Angela DeMichele, Britton Chance, Simon R. Arridge, Martin Schweiger, Joseph P. Culver, Mitchell D. Schnall, Mary E. Putt, Mark A. Rosen, Arjun G. Yodh. 2009. Differentiation of benign and malignant breast tumors by in-vivo three-dimensional parallel-plate diffuse optical tomography. *Journal of Biomedical Optics* **14**:2, 024020. [CrossRef]
10. Mark W. Dewhirst, Yiting Cao, Benjamin Moeller. 2008. Cycling hypoxia and free radicals regulate angiogenesis and radiotherapy response. *Nature Reviews Cancer* **8**:6, 425-437. [CrossRef]
11. Harold M. Swartz . 2007. On Tissue Oxygen and Hypoxia. *Antioxidants & Redox Signaling* **9**:8, 1111-1114. [Citation] [Full Text PDF] [Full Text PDF with Links]